Supporting Information for

Nanoscale Gap-Plasmon-Enhanced Superconducting Photon Detectors at Single-Photon Level

Jing-Wei Yang,[1,2] Tzu-Yu Peng,[1,2] Daniel D. A. Clarke,[3] Frank Daniel Bello,[3] Jia-Wern Chen,[1] Hao-Chen Yeh,[4] Wei-Ren Syong,[1] Chi-Te Liang,[2,4] Ortwin Hess,[3,5]* and Yu-Jung Lu[1,2]*

[1] *Research Center for Applied Sciences, Academia Sinica, Taipei, Taiwan*
[2] *Graduate Institute of Applied Physics, National Taiwan University, Taipei, Taiwan*
[3] *School of Physics and CRANN Institute, Trinity College Dublin, Dublin 2, Ireland*
[4] *Department of Physics, National Taiwan University, Taipei 10617, Taiwan*
[5] *Blackett Laboratory, Imperial College London, South Kensington Campus, SW7 2AZ London, United Kingdom*

*To whom correspondence should be addressed.

E-mail: yujunglu@gate.sinica.edu.tw (Y.J.L.); Ortwin.Hess@tcd.ie (O.H.)

Table of contents

Note S1. Device fabrication

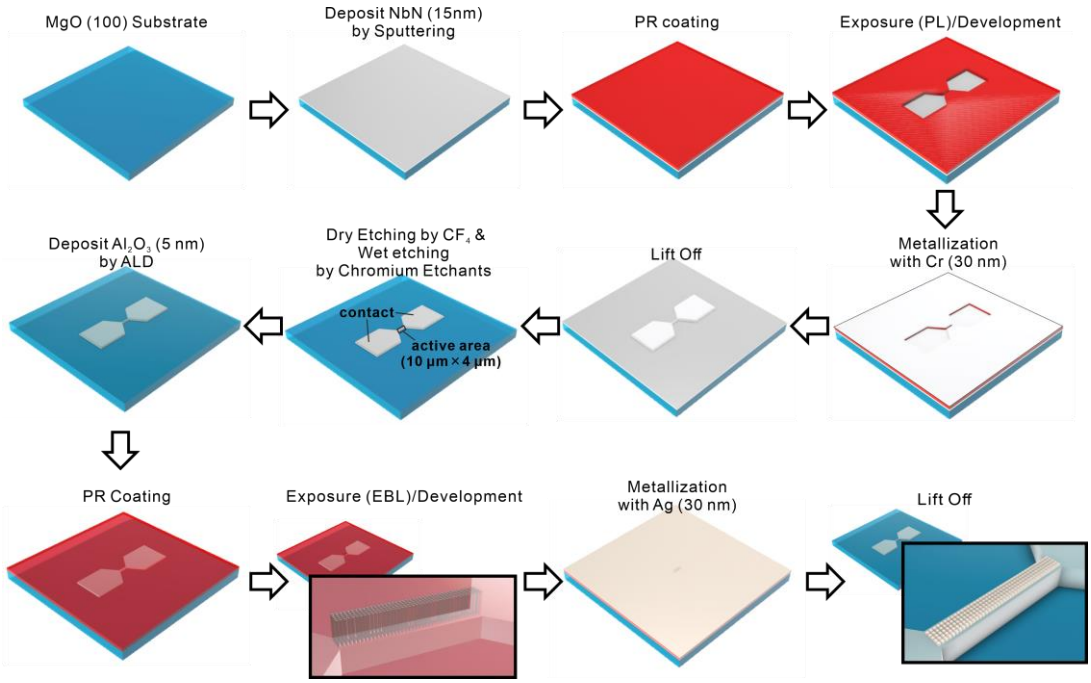

Figure S1 The fabrication flowchart for plasmonic NbN SMPD.

Step 1: Prepare a clean MgO (100) substrate.

Step 2: Deposit a 15 nm-thick NbN film on the MgO (100) substrate at a substrate temperature of 800 ℃.

Step 3: Spin-coat a photoresist (KL5310) layer on the sample and rotate for 10 s with a spin angular velocity of 500 rpm, followed by 45 s with 3000 rpm.

Step 4: Use standard photolithography process to define the pattern of NbN microstrips.

Step 5: Deposit a 30 nm-thick Cr film as a hard mask for dry etching.

Step 6: Perform a lift-off process.

Step 7: Dry etch the unwanted NbN for 40s using CF4, and wet etch the Cr hard mask for 30 s using chromium etchant.

Step 8: Deposit a 5 nm-thick Al2O3 by atomic layer deposition (ALD) for the fabrication of Ag nanocubes array on top of the fabricated NbN microstrips.

Step 9: Spin-coat a photoresist (ZEP520A) on the sample and rotate for 10 s with a spin angular velocity of 500 rpm, followed by 45 s with 3000 rpm.

Step 10: Use electron-beam lithography process.

Step 11: Deposit a 40 nm-thick Ag film by electron-beam evaporation (ULVAC E-beam Evaporator, Peva-400E).

Step 12: Lift off the residual ZEP520A with ZDMAC.

Note S2. Optimization of plasmonic nanostructures that support gap-plasmon resonances at a wavelength of 532 nm

The optical field distributions were calculated with the finite-difference time-domain (FDTD from Lumerical Solutions, Inc.) method. The refractive indices of NbN and Al_2O_3 are obtained from spectroscopic ellipsometry. An ideal structure of an AgNC with sharp edges was considered, and the Courant number was set as 0.99. Plus, the material property of silver is based on the empirical data of P. B. Johnson and R. W. Christy[1]. In the case of normal incidence, a plane wave was shining on a single unit cell of the AgNC array with periodic boundary conditions in the in-plane (*x*-*y*) directions and perfectly matched layer (PML) boundary conditions in the excitation (*z*) direction. The optimized meshing with the minimum mesh size of 3 nm/1 nm covered the whole gap plasmon nanostructure. The results were obtained after the simulation had converged (Figure S2 to Figure S4).

In addition, the absorption of this gap plasmonic mode can be obtained by calculating the divergence of the Poynting vector[2], which is mainly distributed in the NbN substrate and at the bottom of the AgNC.

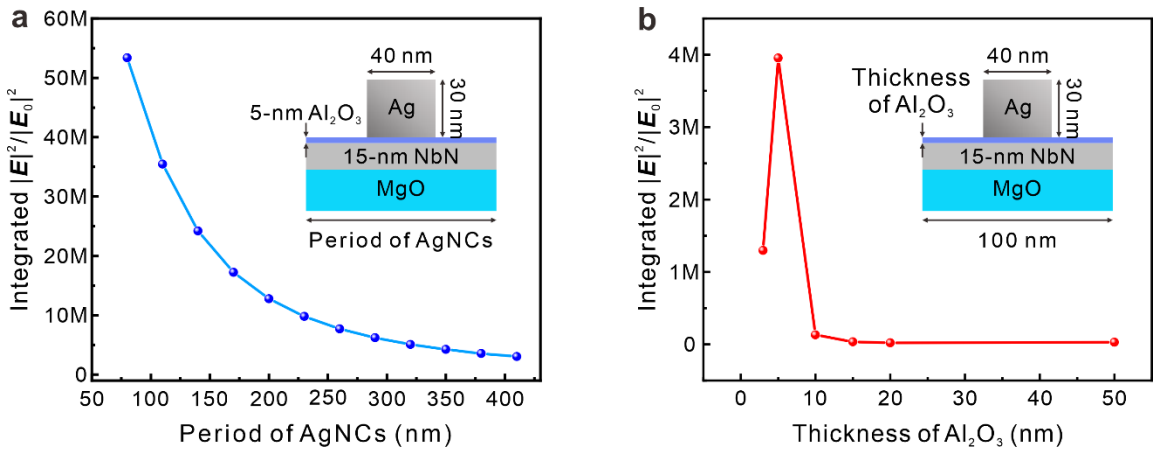

Figure S2 Optimization of the localized electromagnetic field enhancement in the Al_2O_3 layer. (**a**) The total intensity of hot spots excited by a normally incident plane wave at 532 nm as a function of the period of the AgNCs array, where the total intensity is the integrated $|\mathbf{E}|^2/|\mathbf{E_0}|^2$ in the Al_2O_3 layer multiplied by the number of AgNCs covered by the laser spot. (**b**) The integrated $|\mathbf{E}|^2/|\mathbf{E_0}|^2$ of a single hot spot in the Al_2O_3 layer excited by a 532 nm normal incident plane wave while varying the thickness of the Al_2O_3 gap. Insets show the single unit cell of the designed gap plasmon nanostructure.

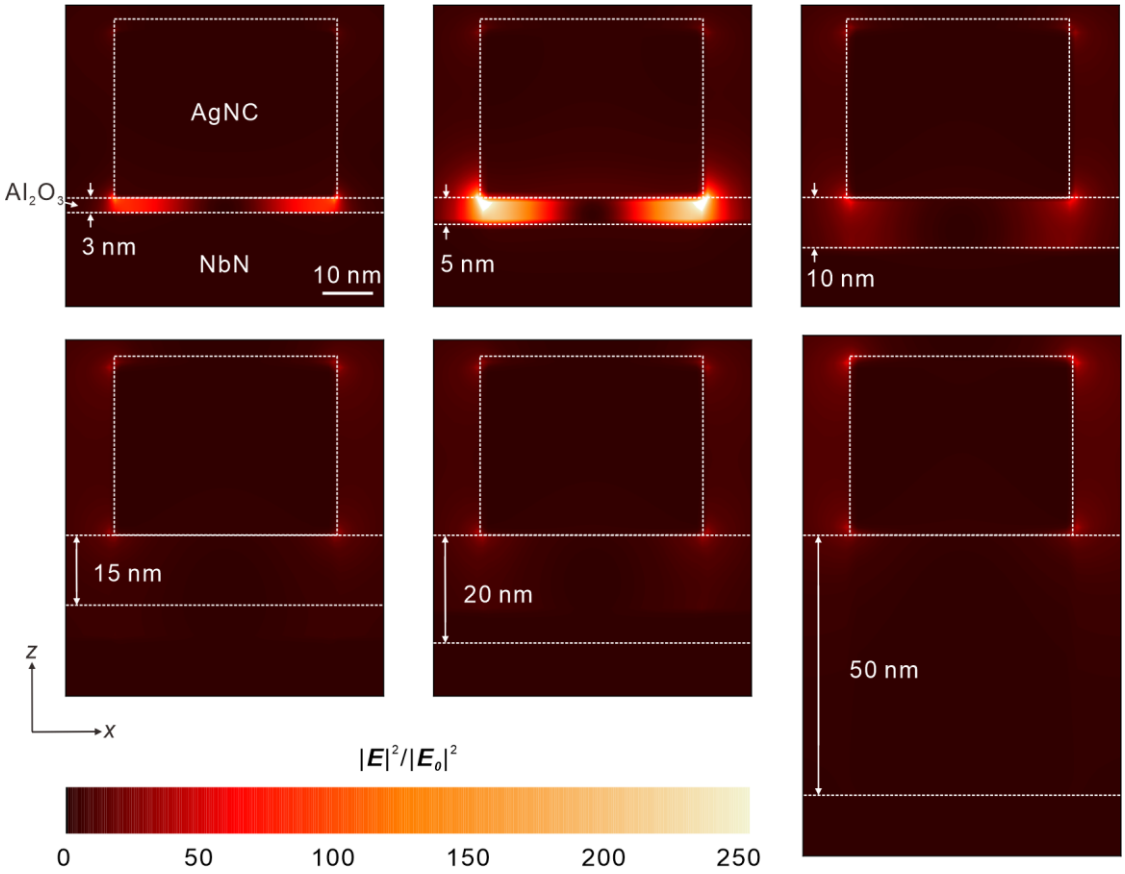

Figure S3 Effectively control the local hot spot in the AgNC/Al_2O_3/NbN plasmonic structures by tailoring the geometric parameters. The calculated $|\boldsymbol{E}|^2/|\boldsymbol{E_0}|^2$ profiles excited by normally incident plane wave at 532 nm. In general, the smaller gaps between two metals will result in stronger localized field. The simulation results indicate that 5 nm-thick Al_2O_3 dielectric gap has relatively strong localized electromagnetic field confinement.

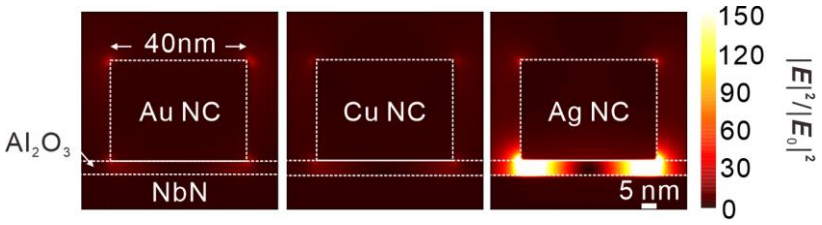

Figure S4 Calculated $|\boldsymbol{E}|^2/|\boldsymbol{E_0}|^2$ profiles for the varied plasmonic nanostructures excited by a normal incident plane wave at 532 nm. A material-dependent local electromagnetic field confinement between the metal nanoparticle (Au, Cu, and Ag) and the NbN film was observed. Among the three metals, the particle-on-film nanocavities based on Ag NC result in strong EM field confinement in the gap between the metal particle and the NbN film.

Note S3. Sample preparation and optical characterization of quasi-epitaxial NbN films

Based on our previous work[3], the properties of the NbN film can be varied with the argon/nitrogen flow rate, target, RF power, and growth temperature. We sputtered NbN film on MgO (100) and Sapphire (0001) substrate with RF magnetron sputtering at a chamber pressure of < 8×10^{-9} Torr and at 800 °C. The detailed growth parameters show in Table S1.

Substrate	**MgO (100)**	**Sapphire (0001)**
Epsilon near zero (*ENZ*) point (nm)	345 nm	360 nm
Ellipsometry fitting model	1 Drude and 2 Lorentz oscillators	1 Drude and 2 Lorentz oscillators
Target	NbN	NbN
Optical property	Plasmonic	Plasmonic
Film thickness (nm)	62	62
Applied Power (W)	RF: 120 W	RF: 120 W
Ar (sccm)/N_2 (sccm) flow rate	12/0.5	12/0.5
Base Pressure (Torr)	3.9×10^{-9}	3.9×10^{-9}
Gas pressure (mTorr)	3	3
Growth temperature (°C)	800	800

Table S1 Material properties and growth parameters of NbN films. The optical properties of the NbN films are strongly related to the growth substrates.

The complex permittivity ε of NbN films can be described by a Drude-Lorentz model measured by using variable angle (65°, 70° and 75°) spectroscopic ellipsometry (VASE, J.A. Woollam Co.). The mean-square error (MSE) of all samples is less than 5%. The measured data by VASE were fitted according to a Drude-Lorentz model, characterized by the sum of a Drude term and two Lorentz oscillators:

$$\varepsilon_{NbN}(\omega) = \varepsilon_{\infty} - \frac{\omega_p^2}{(\omega^2 - i\Gamma_D\omega)} + \sum_{j=1,2} \frac{f_j\omega_{0j}^2}{\omega_{0j}^2 - \omega^2 + i\gamma_j\omega} \quad \text{(S1)}$$

The first and second term are given by the Drude model, which contains three free parameters: the damping factor Γ_D, plasma frequency ω_p, and permittivity in the high-frequency limit ε_∞. The third term is given by the Lorentz model, which contains three fitting parameters: the oscillator strength f_j, the damping factor γ_1, and the oscillator position $\omega_{0,1}$. Here, the index j enumerates the Lorentz oscillators (j=1,2). Table S2 summarizes the values of the obtained fitting parameters that have been used to produce Figure 2a.

Substrate	*ENZ*	ω_p (eV)	Γ_D (eV)	f_1	$\omega_{0,1}$ (eV)	γ_1 (eV)	f_2	$\omega_{0,2}$ (eV)	γ_2 (eV)	ε_∞
MgO	345 nm	9.8	1.8	1535	0.13	0.52	3.2	5.7	2.0	3.0
Sapphire	360 nm	9.6	2.5	867.8	0.14	0.54	3.1	5.9	2.8	2.3

Table S2 The Drude-Lorentz fitting parameters for the complex permittivity of NbN films on different substrates.

Note S4. XRD pattern of NbN film on sapphire

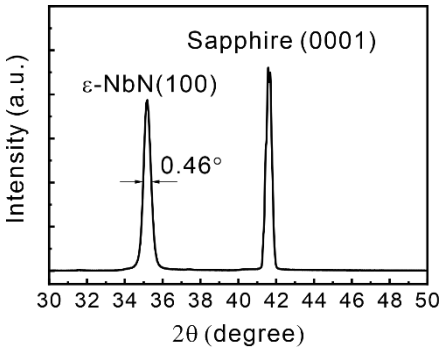

Figure S5 XRD pattern of NbN film on sapphire (0001). The crystal phase of NbN deposited on sapphire (0001) is the ε-phase, which corresponds to a lower T_c than the δ-NbN.

Note S5. SQUID measurements of NbN film

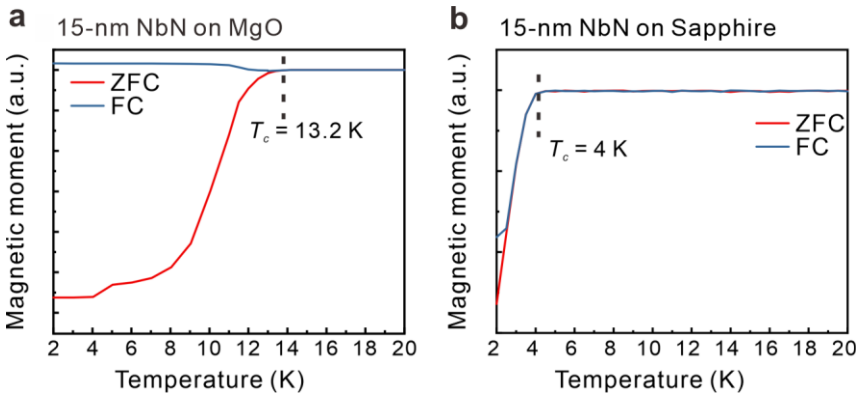

Figure S6 The Zero-field-cooled (ZFC) and field-cooled (FC) magnetization measurements of the 15 nm-thick NbN film to define the critical temperature. (**a**)The critical temperature of NbN film on MgO was measured by SQUID (MPMS3 SQUID magnetometer), which indicates T_c is about 13.2 K. (**b**) The NbN film on sapphire with a low T_c at 4 K.

Note S6. Wavelength dependent photoresponse of the pristine and the plasmonic NbN SMPDs

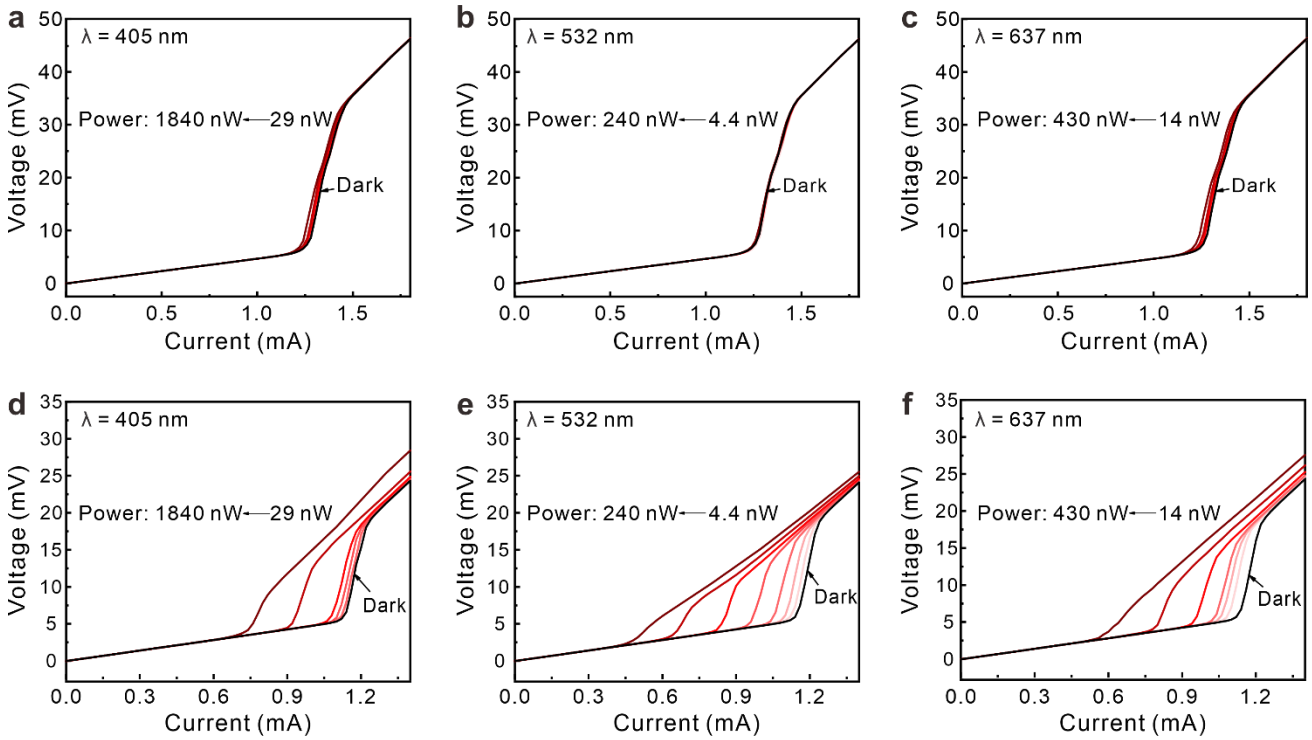

Figure S7 Illuminated power dependent *IV*-curves of pristine NbN SMPDs and plasmonic NbN SMPDs at different wavelengths from blue to red. (**a**)-(**c**) photoresponse of pristine NbN SMPD exhibits a critical current of 1.28 mA, which is insensitive to both the illuminated powers and the photon energy. (**d**)-(**f**) Giant nonlinear photoresponse of plasmonic NbN SMPD exhibits a critical current of 1.13 mA.

Note S7. Wavelength dependent phonon-electron interaction factor

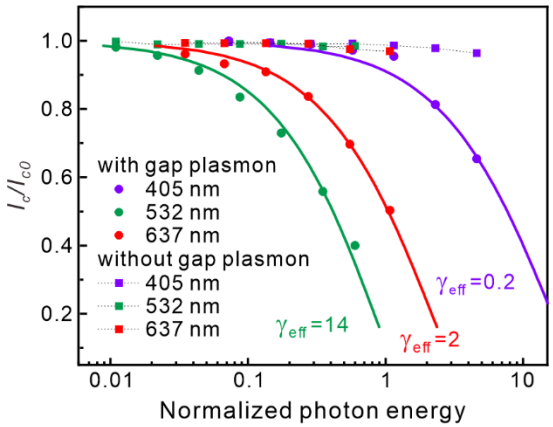

Figure S8 The relation between the detection photoresponse and different photon energy fitted by hot-belt model. The plasmon-enhanced photoresponse can be observed. The calculated wavelength dependent phonon-electron interaction factor γ_{eff} are 0.2, 2 and 14 for wavelength at 405 nm, 532 nm and 637 nm, respectively.

Note S8. Simulation results of electromagnetic heating

The steady-state temperature distribution of the microwire device throughout a two-dimensional cross-section is determined using finite-element methods [4]. In particular, we solve the thermal diffusion equation,

$$\rho C_p \boldsymbol{u}\cdot\nabla T+\nabla\cdot\boldsymbol{q}=Q, \quad \text{(S2)}$$

in which ρC_p is the volumetric heat capacity, $\boldsymbol{u}$ is a unit vector, and Q quantifies the resistive heating source, i.e. power loss in the structure [5]. $\boldsymbol{q}$ is the heat flux whose divergence is given by $-k\nabla^2 T$, where k is the thermal conductivity of each material. Please see Table S3 for a full list of parameters used. Of note, the thermal conductivity of a Ag nanocube is anticipated to be much smaller than values for bulk Ag. We base our estimated value on previous reductions to the thermal conductivity by a factor between 1/2 and 1/3 for thin metallic films below 100 nm in thickness.

Under 70 nW/μm^2 and 220 nW/μm^2 illumination, we find that electric-field enhancements may be on the order of 10^2, but values for energy fluxes are on the order of 10^{-3} nW/nm^2 in the region of enhancement, which correspond to temperature rises that are typically on a milli-Kelvin or smaller scale given the amount of absorbed power and estimated thermal capacities/conductivities (See Table S3). As such, the amount of heating in the NbN region is largely determined by the manner in which the cryogenic head and illumination power dictate the temperatures of the surrounding media. A more substantial temperature rise is predicted under the much higher illumination intensity of 1800 nW/μm^2, as shown in Figure 3e. In this case, a transition from the superconducting to the normal state of NbN is expected.

Material	Vol. Heat Capacity ($J \cdot m^{-3} K^{-1}$)	Thermal Conductivity ($W \cdot m^{-1} K^{-1}$)	Refractive Index (532 nm)
Ag NC	2.4675×10^6	128.7	0.054+3.429i
MgO	3.1572×10^6	42	1.74
Al_2O_3	3.476×10^6	1.3	1.4
NbN	1.0164×10^4	6.0	1.63+3.21i

Table S3 Material parameters employed for the finite-element electromagnetic heating simulations reported in Figure 3d and 3e. The refractive indices (at 532 nm) of MgO, Al_2O_3 and NbN have been measured by spectroscopic ellipsometry, whilst that of Ag has been obtained from the data of Johnson and Christy [1]. Properties of NbN have been taken from available literature [5-9].

Note S9. Measurement of photon-detection efficiency

A pulsed laser with a wavelength of 532 nm (LDH-P-FA-530, PicoQuant), a pulse width of 100 ps, and a repetition rate of 2.5 MHz was used, and the input photon flux was attenuated to five photons per pulse (33 nW/μm^2). The calculation results show that NbN wire is heated from 9 K to 9.89 K under an illumination intensity of 33 nW/μm^2. Hence, the temperature change induced by five photons results in a 26% alteration in the critical current can be estimated (see **Note S8**). The measured temperature was fixed at 0.64 T_c. The readout system includes a bias tee (ZFBT-4R2GW+, Minicircuits) that enables simultaneous biasing of the SMPD detector and RF output signal. A low noise amplifier (LNA-1030, RFBAY) with a 30 dB gain and a noise figure of 2.0, and filters (20 MHz high pass filter, SHP-20+, Minicircuits) are employed to improve the signal-to-noise ratio. The final signal is digitized by an oscilloscope (MDO3054, Tektronix) with a 1.5 GHz bandwidth and four channels sharing a sampling rate of 2.5 GS/s (10,000 events per sample).

Note S10. Overview of performance metrics of superconducting photon detectors

Methods	Enhancement of optical response	Working wavelength (nm)	Working temperature (K)	Ref.
Oscillating magnetic field	3	1064	2.1	Hakimi I., *et al.* [10]
Defect engineering	1.88	1550	2.2	Zhang W., *et al.*[11]
DBR	1.12	1550	1.8	Zhang W., *et al.*[12]
Ag nanoantenna	2.3	1525	3.5	Heath R.M., *et al.* [13]
Series attenuator	6	1550	2.2	Lv C., *et al.* [14]
GPR	11.1 233 25	405 532 637	9	This work

Table S4 Improving the device performance of the superconducting photon detectors through diverse structural optimizations.

Supplementary References

(1) Johnson, P. B.; Christy, R. W. Optical constants of the noble metals. *Phys. Rev. B* **1972,** 6, (12), 4370–4379.

(2) Sun, J.; Hu, H.; Xu, Y.; Li, Y.; Xu, H., Revealing the photothermal behavior of plasmonic gap modes: Toward thermostable nanocavities. *Laser & Photon. Rev.* **2022,** *16*, (5), 2100564.

(3) Karl, P.; Mennle, S.; Ubl, M.; Flad, P.; Yang, J.-W.; Peng, T.-Y.; Lu, Y.-J.; Giessen, H., Niobium nitride plasmonic perfect absorbers for tunable infrared superconducting nanowire photodetection. *Opt. Express* **2021,** *29*, (11), 17087–17096.

(4) COMSOL AB, S., COMSOL Multiphysics TM v.6.0, www.comsol.com.

(5) Yang, J. K. W.; Kerman, A. J.; Dauler, E. A.; Anant, V.; Rosfjord, K. M.; Berggren, K. K., Modeling the electrical and thermal response of superconducting nanowire single-photon detectors. *IEEE Transactions on Applied Superconductivity* **2007,** *17*, (2), 581–585.

(6) Semenov, A. D.; Gol'tsman, G. N.; Korneev, A. A., Quantum detection by current carrying superconducting film. *Physica C: Superconductivity* **2001,** *351*, (4), 349–356.

(7) Lee, S.-M.; Choi, W.; Kim, J.; Kim, T.; Lee, J.; Im, S. Y.; Kwon, J. Y.; Seo, S.; Shin, M.; Moon, S. E., Thermal conductivity and thermal boundary resistances of ALD Al_2O_3 films on Si and sapphire. *International Journal of Thermophysics* **2017,** *38*, (12), 176.

(8) Optical materials, https://www.crystran.co.uk/optical-materials. **1993**.

(9) Lugo, J. M.; Oliva, A. I., Thermal properties of metallic films at room conditions by the heating slope. *J. Thermophysics and Heat Transfer* **2015,** *30*, (2), 452–460.

(10) Hakimi, I.; Vardi, N.; Sharoni, A.; Rosenbluh, M.; Yeshurun, Y., Enhancement of photon detection in superconducting nanowire single photon detector exposed to oscillating magnetic field. *Appl. Phys. Lett.* **2021,** *118*, (23), 232603.

(11) Zhang, W.; Jia, Q.; You, L.; Ou, X.; Huang, H.; Zhang, L.; Li, H.; Wang, Z.; Xie, X., Saturating intrinsic detection efficiency of superconducting nanowire single-photon detectors *via* defect engineering. *Phys. Rev. A* **2019,** *12*, (4), 044040.

(12) Zhang, W.; You, L.; Li, H.; Huang, J.; Lv, C.; Zhang, L.; Liu, X.; Wu, J.; Wang, Z.; Xie, X., NbN superconducting nanowire single photon detector with efficiency over 90% at 1550 nm wavelength operational at compact cryocooler temperature. *Science China Physics, Mechanics & Astronomy* **2017,** *60*, (12), 120314.

(13) Heath, R. M.; Tanner, M. G.; Drysdale, T. D.; Miki, S.; Giannini, V.; Maier, S. A.; Hadfield, R. H., Nanoantenna enhancement for telecom-wavelength superconducting single photon detectors. *Nano Lett.* **2015,** *15*, (2), 819–822.

(14) Lv, C.; Zhang, W.; You, L.; Hu, P.; Wang, H.; Li, H.; Zhang, C.; Huang, J.; Wang, Y.; Yang, X.; Wang, Z.; Xie, X., Improving maximum count rate of superconducting nanowire single-photon detector with small active area using series attenuator. *AIP Adv.* **2018,** *8*, (10), 105018.